

Spectral restoration for femtosecond spectral interferometry with attosecond accuracy

Michael K. Yetzbacher, Trevor L. Courtney, William K. Peters, Katherine A. Kitney, Eric Ryan Smith, and David M. Jonas*

Department of Chemistry and Biochemistry, University of Colorado, Boulder, Colorado 80309-0215, USA

**Corresponding author: David.Jonas@colorado.edu*

Received November 5, 2009; revised March 5, 2010; accepted March 5, 2010;
posted March 8, 2010 (Doc. ID 119613); published April 29, 2010

A spectral restoration algorithm appropriate for the asymmetric and wavelength-dependent linespread of broadband spectrographs with pixelated detectors is presented. The algorithm's accuracy was tested on spectra of femtosecond pulse pairs with known delays from an actively stabilized interferometer. Using interleaved atomic line spectra, the spectrograph calibration and effective linespread function were retrieved with sub-pixel accuracy. The spectral restoration by Fourier pseudo-deconvolution with the effective linespread function reduced systematic artifacts and allowed recovery of the phase delay to ± 2.4 as over a 2 ps range (± 0.7 nm path differences over 0.6 mm). The slope delay was determined to within ± 20 as and constant (intercept) phase shifts to within ± 0.05 rad; these accuracies are limited by Fourier filtering of charge coupled device and interferometer imperfections. © 2010 Optical Society of America

OCIS codes: 320.7100, 120.3180, 120.5050, 110.4850, 120.6200, 100.3020.

1. INTRODUCTION

Spectral interferometry determines the phase difference between two mutually coherent beams of light from the frequency domain power spectrum of the superposed beams [1–15]. It has long been known that the interference in the frequency spectrum of the output of white light interferometers provides a single frame measurement of displacement [1,2,16]. Spectral interferometry is unique in its ability to measure time delays and constant spectral phase shifts between ultrafast pulses [11,12]. This allows the single shot measurement of constant (carrier-envelope) phase shifts [17,18]. Such measurements are also essential to distinguish, for example, a photon echo (observed for inhomogeneous broadening, where an excitation pulse time delay produces a signal time delay) from a nonlinear free induction decay (observed for homogeneous broadening, where an excitation pulse time delay produces a constant phase shift of the signal) and in two-dimensional spectroscopy [19]. Spectral interferometry is widely used in pulse characterization [20], characterization of optical components [21], surface profiling [6,7,15], and optical coherence tomography [22]. The independent measurement of optical path lengths and phase shifts could be powerful in these applications as well; for example, by separating the optical path length to the surface from the material dependent phase shift on reflection, spectral interferometry could accurately profile height for surfaces covered by more than one material.

Algorithms for evaluating the spectral phase have been crucial for improving the precision and accuracy of spectral interferometry. White light spectral interferometry and multi-point phase-retrieval algorithms have been used to measure path length differences with a precision of 1 nm over a range of 5 μm [7]. Fourier transform algo-

gorithms effectively exploit the entire spectrum [3–5,8,9]. Dorrer [10] used Fourier transform spectral interferometry (FTSI) to determine the nonlinear calibration error of a spectrograph. Since the data are unevenly sampled in the frequency domain, the order of Fourier transformation and interpolation is crucial for time domain accuracy [11,13]. Joffre and co-workers [13] measured the modulation transfer function (MTF) of a spectrograph and compared the MTF with the Fourier transform of an atomic line spectrum. After accounting for these effects on the measurement, the group delay dispersion (GDD) was measured with improved precision ($\sim 0.25 \text{ fs}^2$) [10,14,23] and an accuracy within the experimental error of $\sim 1 \text{ fs}^2$ (which may be due to uncertainties in the Sellmeier coefficients and path length for the dispersive material) [10]. Recently, Debnath *et al.* [15] demonstrated a 20 nm accuracy for optical path differences using the basic FTSI algorithm of [3,5,8]. The accuracy of the algorithms for spectral interferometry has not, to our knowledge, been experimentally tested for the constant phase term.

Accurate spectral interferometry requires the restoration of the incident spectrum from the measured spectrum using the effective linespread function (eLSF) and frequency calibration of the spectrometer and pixelated detector. The eLSF incorporates the line broadening, shift, and sampling effects of the spectrometer and the pixelated detector. In this sense, the measurements of [13] retrieve the effective MTF which is the magnitude of the Fourier transform of the eLSF. We describe a general method of determining the eLSF and demonstrate its utility by recovering phases from spectral interferograms with a root mean square (rms) phase delay error of ± 2.5 attoseconds (as) for a wavelength dependent, asymmetric eLSF with spatial frequency components above the Nyquist limit imposed by detector pixelation. This accu-

racy depends on spectral restoration, analogous to image restoration. We also introduce pseudo-deconvolution as a fast spectral restoration algorithm for an eLSF which is shift invariant over its range of support.

2. THEORY

The spectral irradiance (spectrum) of two superposed beams of mutually coherent light is

$$I(\omega) = e_1(\omega)^2 + e_2(\omega)^2 + 2e_1(\omega)e_2(\omega)\cos[\Delta\phi(\omega)], \quad (1)$$

where ω is the angular frequency, $e_i(\omega)$ ($i=1,2$) is a real-valued amplitude for each beam, and $\Delta\phi(\omega)=\phi_1(\omega)-\phi_2(\omega)$ is the phase difference. For coherent pulses of light, $\hat{E}(\omega)=e(\omega)\exp[i\phi(\omega)]$ is proportional to the complex-valued frequency domain electric field with spectral envelope, $e(\omega)$, and spectral phase, $\phi(\omega)$. An ideal interferogram has a fringe depth of $4|e_1e_2|$ and upper (lower) envelopes of $e_1^2+e_2^2+(-)2|e_1e_2|$. For blurred interferograms, the fringe visibility, \hat{V} , defined by the fringe depth/(upper envelope+lower envelope) is less than the ideal fringe visibility, $V_{\text{ideal}}=2|e_1e_2|/(e_1^2+e_2^2)\leq 1$. The intensity in the frequency domain is usually measured by using the spatial domain to encode the wavelength (λ) domain. The irradiance, I_p , measured by a pixel p of a pixelated detector in a wavelength resolving system is an integral of the product of the incident spectral irradiance $I(\lambda)$ with S_p , the spectrograph determined sensitivity of pixel p :

$$I_p = \int_0^\infty d\lambda I(\lambda)S_p(\lambda_p - \lambda). \quad (2)$$

In general, the real and positive sensitivity, S_p , of each pixel can be determined by either Fourier transform spectroscopy with a fully characterized interferometer and known incident spectrum or by tuning a sufficiently narrowband source. Viewed as a function of p and λ , the set of sensitivities $S_p(\lambda_p - \lambda)$ in Eq. (2) is a kernel for the linear integral transformation from the continuous spectral irradiance $I(\lambda)$ into the discrete spectrum I_p ; Eq. (2) is not a convolution when S_p depends on p .

The methods developed here are applicable to spectrographs with uniformly pixelated detectors and slow variation in S_p with p . Extending the calibration relation, $\lambda_p(p)$, to real values of a pixel variable, \mathcal{P} , and substituting into the sensitivity, gives $S_p(\lambda_p - \lambda) = s_p(p - \mathcal{P})$, the eLSF. By analogy to the effective point-spread function [24] the eLSF incorporates both the linespread of the spectrometer and the pixelation of the detector. In general, spectral restoration can be accomplished by image restoration methods such as the Richardson–Lucy algorithm [25], singular value decomposition [26], or coordinate transformation [27]. For the special case where $s_p = s$ for all p , I_p is a convolution of I with s and spectral restoration can be accomplished by deconvolution. The Fourier transform with respect to \mathcal{P} of the eLSF is the complex-valued effective optical transfer function (OTF, \hat{T}):

$$\hat{T}_p^{\text{eff}}(\xi) = \int_{-\infty}^{\infty} s_p(\mathcal{P})e^{-i\xi\mathcal{P}}d\mathcal{P}. \quad (3)$$

We refer to the ξ domain [13] as “quasi-time” [11]. Here, ξ is the Fourier conjugate to the pixel number (rather than the Fourier conjugate to the wavelength as in [11,13]) because the wavelength is a nonlinear function of the known pixel numbers. The absolute magnitude of \hat{T} is the MTF (MTF= $|\hat{T}|$). The MTF completely describes s_p if s_p is symmetric. The discrete Fourier transform of the measured irradiance with respect to p is given by

$$\hat{I}_\xi = \sum_{p=0}^{N-1} I_p e^{-i\xi p} \Delta p, \quad (4)$$

where N is the number of pixels and $\Delta p=1$. When s_p does not vary with p over its range of support, the restored discrete spectrum is

$$I_p^0 = \frac{1}{2\pi} \sum_{n=0}^{N-1} \frac{\hat{I}_\xi}{\hat{T}_p^{\text{eff}}(\xi)} e^{i\xi p} \Delta \xi, \quad (5)$$

where $\xi=2\pi n/N$. Since $\Delta\xi=2\pi/N$, when $\hat{T}_p^{\text{eff}}(\xi)=1$, Eqs. (4) and (5) become the standard discrete Fourier transform of [28]. When $\hat{T}_p^{\text{eff}}(\xi)=\hat{T}^{\text{eff}}(\xi)$ is independent of p , Eq. (5) becomes a discrete deconvolution. The restored spectral irradiance is

$$I_0(\lambda_p) = \left(\left. \frac{d\lambda}{d\mathcal{P}} \right|_{\mathcal{P}=p} \right) I_p^0, \quad (6)$$

where $(d\lambda/d\mathcal{P}|_{\mathcal{P}=p})$ is the Jacobian transformation from the pixel to wavelength space evaluated at $\mathcal{P}=p$, which is evaluated here using the quadratic calibration relation

$$\lambda(\mathcal{P}) = c_0 + c_1 \left(\mathcal{P} - \frac{N}{2} \right) + c_2 \left(\mathcal{P} - \frac{N}{2} \right)^2, \quad (7)$$

where c_0 , c_1 , and c_2 are experimental calibration constants referenced to the middle pixel ($N/2$).

We call the spectral restoration algorithm based on Eq. (5) pseudo-deconvolution. If s_p has a full width at half maximum (FWHM) of less than 2 pixels, it is considered “undersampled” [29]. The numerical application of Eq. (3) to an s_p undersampled on the grid p will produce aliasing in $\hat{T}_p^{\text{eff}}(\xi)$. The sampling of s_p in \mathcal{P} at intervals smaller than one pixel allows Fourier transformation to $\hat{T}_p^{\text{eff}}(\xi)$ without aliasing. The spectrum I must be adequately sampled in p to avoid aliasing in \hat{I}_ξ . In order to get $I_0(\lambda_j)$ for the one pixel $p=j$, we deconvolve the entire discretely measured spectrum, I_p in Eq. (2), with the eLSF at that pixel, s_j , using Eq. (5). This deconvolution, which is different for each pixel, is repeated for every pixel to approximately reconstruct the incident spectrum. An unstable division in Eq. (5) is avoided because the eLSF is undersampled in p ; $\hat{T}_p^{\text{eff}}(\xi)$ has no zeros over the range of quasi-time sampled by \hat{I}_ξ from the grid p . Therefore, Fourier deconvolution of an adequately sampled (in p) spectrum with an adequately sampled (in \mathcal{P}) eLSF that is un-

dersampled on p does not have the extreme signal to noise requirements often associated with deconvolution.

The pseudo-deconvolution algorithm was tested using an asymmetric, wavelength dependent eLSF (similar to experiment) for the blurring and restoration of interferograms resembling those of the experiment [ideal interferograms with $\Delta\phi(\omega)=\omega\tau$ were calculated for time delay between pulses, τ , ranging from 0 to 2500 fs], which produced experimentally negligible errors. Blurring and restoration were also performed using an asymmetric eLSF with exaggerated widths and wavelength dependence, which revealed the limitations of the algorithm.

Figure 1 shows an exaggerated example, in which the interferogram fringe visibility is reduced about twofold at 500 fs delay (with ~ 8.5 pixels/fringe) by an eLSF that ranges from 2 to 3.4 pixels wide [30]. The ideal interferogram is calculated from Eq. (1) for two identical pulses. The wavelength dependent eLSF, shown for 3 pixels, becomes wider and more asymmetric for shorter wavelengths. As a result, the blurred interferogram calculated with Eq. (2) has a lower fringe visibility for shorter wavelengths. Furthermore, a careful inspection of Fig. 1 shows that the blurred interferogram fringes are increasingly shifted to shorter wavelengths by the increasing asymmetry of the eLSF at shorter wavelengths. The spectral restoration using the pseudo-deconvolution algorithm of Eq. (5) leads to points that agree with the ideal interferogram

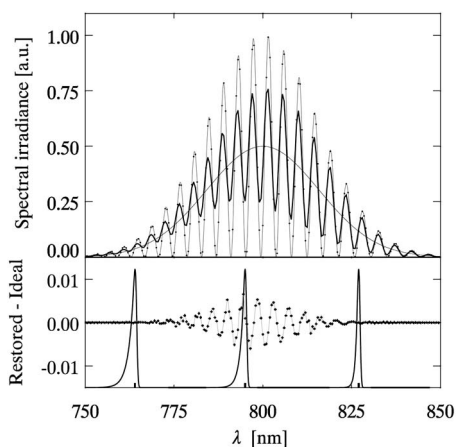


Fig. 1. Simulation to illustrate pseudo-deconvolution for a spectral interferogram with 500 fs delay. Top panel: ideal interferogram $I(\lambda)$ (gray line); blurred interferogram I_p (thick black line) calculated with Eq. (2) for a wavelength dependent asymmetric eLSF, s_p ; spectrum $I_0(\lambda_p)$ as restored by pseudo-deconvolution using Eq. (5) on a 512-pixel array (diamonds); sum of pulse spectra [first two terms of Eq. (1)] (thin black line). Bottom panel: representative asymmetric pixel sensitivity functions S_p (thick black lines) with their pixel centers marked at 764, 795, and 827 nm; difference between restored interferogram and ideal interferogram (crosses) and as interpolated by zero-padding (gray line). The eLSF width increases for shorter wavelengths resulting in decreased fringe depth for the blurred interferogram at shorter wavelength. The fringes in the blurred interferogram are also shifted toward shorter wavelengths with respect to the ideal interferogram; this shift is more pronounced at shorter wavelengths as the eLSF becomes increasingly asymmetric. The restored interferogram is within $\pm 0.6\%$ of the ideal interferogram at every pixel, with a rms error over 750–850 nm of 0.2%. In this exaggerated example, the eLSF is over two times wider than in the experiment and varies ten times more, which magnifies the errors from pseudo-deconvolution by 2 orders of magnitude.

to within $\pm 0.6\%$ (rms error 0.2% over 750–850 nm). The strong wavelength dependence of the wide eLSF in this exaggerated example makes it so that the FWHM of S_p varies by 0.6% over its range of support; this suggests these residuals arise from the extent to which the condition of validity for Eq. (5) is violated. Supporting this hypothesis, the spectral restoration error remains constant with increasing time delay even as the fringe spacing approaches 2 pixels (Nyquist limit), where the fringe depth is reduced by a factor of 20.

Another test of the accuracy of the pseudo-deconvolution algorithm used an eLSF similar to that of the experiment for blurring and restoring calculated interferograms. In this case, the width of the eLSF varied between 1.23 and 1.39 pixels [31], and there are 17 pixels/fringe at 500 fs delay. The spectral restoration by pseudo-deconvolution produced errors in the restored spectra of up to $\pm 0.004\%$ (rms error 0.001% over 750–850 nm). The FWHM of S_p varies by 0.03% over its range of support, which is closer to fulfilling the condition for validity of Eq. (5). The pseudo-deconvolution error is far below the shot noise limit for experiments with $\sim 10^6$ photons/pixel.

The problems of determining the calibration and the eLSF are closely related. The asymmetry in the eLSF can arise from spectrometer coma [32] and makes the separate determination of S_p and λ_p ambiguous; the assignment of a particular wavelength, λ_p , to a feature of the asymmetric function, S_p , cannot be unique. Further, variation in S_p due to aberrations [33] may prevent consistent assignment of λ_p to a reference point in S_p . The pixels may also be unevenly spaced due to step-and-repeat errors in CCD fabrication [34]. In the initial determination of S_p , we assume that the pixels are evenly spaced and that the S_p are invariant over a range of 4 pixels. We determine S_p and λ_p together, assigning λ_p to the maximum of S_p . The ambiguity between S_p and λ_p is removed by using the same S_p in both pseudo-deconvolution and the wavelength calibration used to determine λ_p .

3. EXPERIMENT

In the experiment (Fig. 2), the pulse train from a mode-locked Ti:sapphire laser is sent into a Mach-Zehnder interferometer to generate mutually coherent pulse pairs from each pulse in the train. After the first interferometer beam splitter, the two beams of light propagate along separate optical paths until they are recombined at the second beam splitter. The two output beams from the interferometer have complementary fringe patterns [35] due to the introduction of a π phase shift between the transmitted and reflected beams at each beam splitter [36]; for a loss-less interferometer, the frequency spectra of the two output beams add up to the input frequency spectrum. The pulse pair from the interferometer output beam with a symmetrical path (one beam splitter reflection and one beam splitter transmission for each beam) and a nominal central white fringe [37] at zero delay [$\Delta\phi=0$ in Eq. (1)] is then coupled into a spectrograph. Inside the grating spectrometer, the pulses are temporally stretched to the inverse of the spectrometer frequency resolution, so that they temporally overlap and interfere on the CCD array. The spectrum of the train of interfering

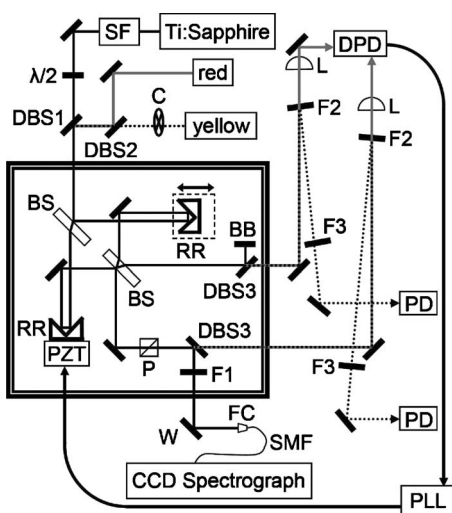


Fig. 2. Stabilized Mach-Zehnder interferometer. One arm of the interferometer has a retroreflector on a computer-controlled motorized translation stage. The other arm's retroreflector is mounted on a PZT, which receives the feedback signal from the difference between the two interferometer outputs for the red CW laser. Stabilization was measured out of loop by monitoring the difference of the two yellow CW laser interferometer outputs. SF: spatial filter; DBS1: dichroic beam splitter (transmits Ti:sapphire; reflects red and yellow CW); C: chopper; DBS2: dichroic beam splitter (transmits yellow CW; reflects red CW); $\lambda/2$: half-wave plate (rotates Ti:sapphire polarization from horizontal to vertical); BS: 50–50 beam splitter, s-polarized; RR: trihedral retroreflector; P: ultrafast plate polarizer with plane of incidence parallel to polarization vector of vertically polarized light (transmits *p*-polarized light); DBS3: dichroic beam splitter (transmits red and yellow CW, reflects Ti:sapphire); BB: beam block; F1: longpass filter (cut-on wavelength: 650 nm); W: window; FC: fiber coupler; SMF: single-mode fiber; F2: red CW bandpass filter (632.8 ± 5 nm); L: plano-convex lens, $f=25.4$ mm; DPD: differential photodiode (for red CW interferometer outputs); F3: yellow CW bandpass filter (600 ± 5 nm); PD: single photodiodes (for yellow CW interferometer outputs); PLL: phase locked loop. Protected silver mirrors are unlabeled.

pulse pairs has the form given by Eq. (1) but is blurred by finite spectrograph resolution according to Eq. (2). The linear intensity spectrum of the interfering pulses is recorded at a single time delay as a function of wavelength and is known as a spectral interferogram. The Fourier transformation of the interferogram in Eq. (1) to the time domain, filtering to select the peak at the pulse delay, and inverse Fourier transformation back to the frequency domain are the basic steps of the FTSI algorithm [5] for amplitude and phase retrieval. Modification is needed for spectral interferograms recorded with a grating spectrometer [11,12] and CCD detector [13].

To test the accuracy of FTSI, both the interferometer and spectrograph are characterized. The red continuous wave (CW) laser intensities from both interferometer outputs are used in the active stabilization of one interferometer arm, while the other arm is adjustable. This active stabilization ensures that the time delay between pulses in each pair is an offset plus an integer number of CW laser periods. The yellow CW laser intensities from both outputs provide an independent check of the interferometer stabilization. For spectrograph calibration accuracy, both the pulse pairs from the interferometer and the atomic line spectra for spectrograph characterization are

coupled into the CCD spectrograph with the same single-mode fiber [19]. The FTSI accuracy attained here requires particular care in the five following areas: the linear read-out of the CCD (Subsection 3.A); calibration of the CCD spectrograph using the measured eLSF (Subsection 3.B); correction for motion of the CCD within the Dewar (Subsection 3.C); construction and stabilization of the interferometer (Subsection 3.D); and ordering of steps in phase retrieval (Subsection 3.E).

A. Recording Data

All calibration spectra and interferograms were recorded by coupling the light through a microscope objective with $NA=0.10$ (Newport M-5X) into a single-mode fiber with $NA=0.13$ (Thorlabs 780HP). The output of the fiber was fed into a 0.34 m Czerny–Turner spectrograph (SPEX 340S, 300 groove/mm grating, $f/4$ optics) with a 256×1024 element, liquid nitrogen cooled, front-illuminated CCD array (Princeton Instruments LN/CCD-1024E) with 16 bit digitization. A front-illuminated CCD was used because higher quantum efficiency back-thinned CCDs exhibit interference fringing (also referred to in the literature as etalon effects) [34]. The CCD has a quantum efficiency of 32%–41% over the pulse spectrum and gain was set to produce one count for every four photoelectrons (~ 10 photons per count). In order to reduce CCD array movement due to cooling, data acquisition began 1 h after the chip reached temperature lock. This particular on-camera shutter was found to perturb the recorded spectrum. While simply holding the shutter open eliminates the perturbation of the spectrum due to shutter motion, charge persistence [38] was observed when the CCD was operated without a shutter. Therefore, an off-camera shutter (Sutter Instrument Co., IQ25) was used to block the beam before the interferometer. The CCD array (e2v technologies CCD30) has $26 \mu\text{m}$ pixels with step-and-repeat errors of $\pm 0.1 \mu\text{m}$ every 15 pixels [39]. The manufacturer's read noise specification is four to six electrons per read. The spectra from each arm of the interferometer were not visually smooth unless the background was subtracted and the background subtracted spectra were divided by a flatfield [29,34]. No correction was made for the slowly varying sensitivity of the detector with wavelength. The smoothness of the spectra was quantified by Fourier transformation of the background subtracted, flatfielded spectra. For each single pulse, \hat{I}_ξ smoothly decayed to $\hat{I}_\xi < \hat{I}(0)/1000$ within 15 quasi-time increments. The apparent “noise” below this level was not suppressible by further averaging. This could arise from CCD electronics (see below), CCD step-and-repeat fabrication errors [34], residual etalon effects in the CCD [34], fine structure in the pulse spectrum (possibly arising from optical coatings [40]), etc.

Preliminary experiments in which interferograms were recorded quickly by binning charge on the chip resulted in a nonlinear response. This nonlinearity was visible as harmonic peaks in the quasi-time domain at $\xi=2\xi_\tau$ and $\xi=3\xi_\tau$ of 0.8% amplitude relative to the main oscillatory peak at the quasi-time delay $\xi=\xi_\tau$. When each harmonic peak is isolated and Fourier transformed back to the pixel domain, the maxima and minima of the nonlinear peaks

do not line up with the maxima and minima from the main oscillation as would be expected from a pure nonlinearity in counts per photon on a given pixel. The nonlinearity shifts the fringe pattern to the side, which indicates coupling between counts arising on different pixels. The phase of the nonlinear peaks, therefore, shows that the nonlinearity involves cross-couplings between pixels, a phenomenon reported previously but not fully understood [41]. In the experiments reported above, this nonlinearity appeared even though the register pixel was filled to only $\sim 30\%$ of full well capacity.

This nonlinearity was minimized by reading pixels individually. The image on the chip was confined to the top 90 rows of the CCD. The images were then taken by reading the upper 90×1024 elements of the detector individually, keeping the intensity and integration time constant, resulting in register pixels being used at less than 1.5% of full well capacity (maximum 1000 counts/pixel). The pixels from the CCD were read out at the slowest possible speed (50 kHz) to minimize the influence of the read noise [29]. Though the data suffers from $\sqrt{90} \times$ larger read noise when each pixel is read individually, this is made up for by the decrease in the nonlinear response. The integration time was 150 ms; ten integrations were added in the CCD software to increase the signal-to-noise ratio. All further data processing used Fortran programs, beginning with an integration over the 90 vertical pixels. An average of the 50 background spectra recorded without illumination throughout data collection (each a sum of ten spectra with 150 ms integration time) was subtracted (several “cosmic ray” hits [29,34] were deleted from the 50 background spectra before averaging). The background spectra (which contain both read noise and dark noise) have a standard deviation of 31 counts (4.1 electrons per pixel read) compared to $\sim 300\,000$ counts at the peak of a spectral interferogram. The column to column variation in pixel sensitivity (flatfield [29,34]) appropriate for fiber illumination was determined by rotating the spectrometer grating to scan the spectrum of a single pulse across the chip in 14 pixel steps and numerically adding these background subtracted spectra. The resulting flatfield has an average of 6×10^6 photoelectrons per pixel (shot noise 0.04%) and reveals long range sensitivity drifts of 7% over the width of the spectrum along with pixel to pixel variations in column integrated sensitivity of 0.7% [42]. Background subtracted spectra were divided by this flatfield (cosmic ray removal was not attempted on spectral interferograms because cosmic ray hits [34] would be obscured by shot noise). Five such interferograms were recorded at each of the 20 interferometer delays between 300 fs and 2 ps. With the register pixel charges minimized as described above, the second harmonic peaks in quasi-time decreased to 0.15% and the third harmonic dropped below the apparent noise floor, which was reduced to 0.03% of the primary oscillatory peak.

B. Recovery of the eLSF/Calibration

The calibration and recovery of the eLSF uses an iterative procedure similar to one used to measure the effective point-spread function of a camera on the Hubble Space Telescope [24]. Here, the spectrometer grating is rotated to dither undersampled atomic line spectra redistributing

the intensity to neighboring pixels and enabling the recovery of the eLSF on a fine grid in \mathcal{P} . In the astrometric measurement [24], distances must be determined from the data, while in the spectrometric measurement, wavelengths (and hence wavelength differences) are known *a priori*. This allows the recovery of the nonlinear (in p) calibration axis of the spectrograph. One hundred emission spectra from an argon lamp (Oriel model 6030) are dithered across four pixels. The spectra of this lamp recorded with a Bomem Fourier transform spectrometer (model DA3.002) show linewidths of less than ~ 0.03 nm at FWHM; the spectrograph’s eLSF has a FWHM ten times greater (~ 0.35 nm or 1.4 pixels). The effect of the finite width of the atomic lines on the width of the eLSF is thus below 0.4% and has been ignored. Each spectrum is the sum of ten acquisitions of 150 ms each. The intensity of the atomic lines falling on the chip was reduced to allow the register pixels to be used at no more than 1.5% of capacity to reduce the effect of the pixel coupling nonlinearity. This yielded integrated line spectra with lines displaying between 104 000 and 2900 counts at their maxima. According to Eq. (2) of [45], the shot noise uncertainty in the center of Gaussian lines with a linespread FWHM of 1.4 pixels at these count levels is between 0.0015 and 0.009 pixels. (A simulation of recorded spectra including read and shot noise with the experimentally recovered eLSF indicated the centering accuracy to be slightly better than for Gaussian line shapes.)

For each spectrum, nine unblended lines [43,44] in a spectral range of ~ 696 – 912 nm are separately fit to approximate line shapes using a nonlinear least-squares procedure [International Mathematical and Statistical Libraries (IMSL) routine DUNLSF, a modified Levenberg–Marquardt algorithm] to yield the nine line maxima, \mathcal{P}_{\max} , at sub-pixel resolution. Each spectrum has a quadratic least-squares fit (using IMSL routine DRCURV) between the nine \mathcal{P}_{\max} and the literature vacuum wavelengths [43], λ_{lit} , which produces a set of three calibration constants in Eq. (7) [46]. All 100 spectra are then interleaved on their wavelength axes. The interleaved sampling of the line shape is at ~ 100 data points between adjacent pixel centers. To this point, the above procedure resembles those used to oversample Raman spectra with pixelated detectors [47,48].

The line shape and calibration depend on the initial guess for the eLSF, so an iteration [24] of the procedure in the above paragraph is used to improve both. Each line shape is defined by a smoothed cubic spline (IMSL routine DCSSCV) centered on λ_{\max} (the wavelength of maximum intensity) which becomes the approximate line shape function in the next iteration. The final (tenth) iteration produces a cubic spline eLSF for each of the nine initial unblended lines, again centered at λ_{\max} . Figure 3 shows the final interleaved spectrum near 764 nm and the fit used as the eLSF for that wavelength. After the final iteration, the nine normalized eLSF line shapes are least squares spline interpolated in wavelength space (IMSL routine DBSLSQ, used in second order) and re-normalized to obtain the smoothly varying eLSF for all 1024 pixels. Figure 4 shows the asymmetric eLSF for two different wavelengths. The widths of the measured eLSF vary by up to 12% from 696–912 nm. Because the eLSF

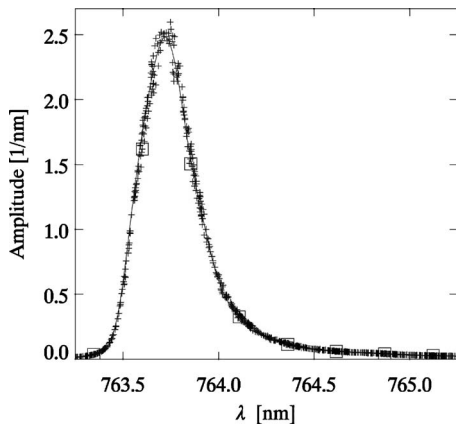


Fig. 3. Atomic line spectra interleaved for the vicinity of $\lambda = 764$ nm (crosses). The open squares are an undersampled set of data points from a single calibration spectrum. The solid line is the smoothed cubic spline fit to the interleaved spectra which is used as the eLSF of the instrument near 764 nm.

contains spatial frequency components above the Nyquist limit of the grid p , its Fourier transform from pixel space would be strongly aliased without sub-pixel sampling; the eLSF for each pixel was sampled at intervals of 1/512 pixel before Fourier transformation to eliminate aliasing in the OTF. The imaginary part of the OTF typically contains 7% of the amplitude, a small but significant asymmetry. The asymmetry of the eLSF is primarily due to the spectrometer (rather than the CCD) as linespread measurements of a HeNe laser with a slit show similar asymmetry.

Error in the eLSF is manifested as systematic trends in the pixel phase error e_p [24],

$$e_p(\mathcal{P}_{\max} - p_{\max}) = \mathcal{P}_{\max} - \mathcal{P}(\lambda_{\text{lit}}), \quad (8)$$

where $\mathcal{P}(\lambda_{\text{lit}})$ is found by inverting the calibration law for each spectrum; $s_p(\mathcal{P})$ is maximized at \mathcal{P}_{\max} ; and $\mathcal{P}_{\max} - p_{\max}$ is the deviation of \mathcal{P}_{\max} from the nearest integer. Equation (8) indicates a procedure for constructing a discrete graph of $\mathcal{P}_{\max} - \mathcal{P}(\lambda_{\text{lit}})$ versus $\mathcal{P}_{\max} - p_{\max}$, not a functional relationship. For each calibration line, the standard deviation of e_p reflects the precision of finding the line centers with the eLSF. This precision improves with

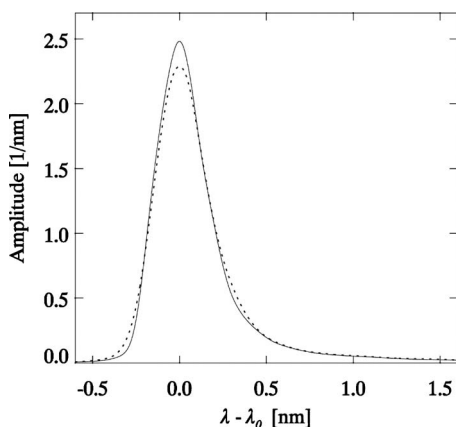


Fig. 4. eLSF in the relative wavelength domain determined at 852 nm (dotted line) and 764 nm (solid line). Each is normalized to have unit area.

iteration, as the average standard deviation of e_p (over all nine lines and 100 spectra) drops from 0.027 pixels on the first iteration to 0.0037 pixels on the tenth. The measured eLSF has a low amplitude tail that allows for more accurate centering than expected from a Gaussian eLSF. Therefore, the average standard deviation observed is slightly better than the rms shot noise limit of 0.004 pixels expected for a Gaussian eLSF of similar FWHM calculated with Eq. (2) of [45]. After the tenth iteration, the changes in the pixel phase error are changes to the constant offset for each line, not the line shape. The removal of constant offsets due to the inability of the smooth calibration function to describe the spectrograph perfectly has a detrimental effect on the interpolated line shapes, so the algorithm is stopped after ten iterations. Such constant offsets could arise either from eLSF variations that change the relation between λ_{\max} and λ_{lit} or from step-and-repeat errors in CCD fabrication. Over the nine lines and 100 spectra, the rms constant offset in e_p is 0.005 pixels, which is only slightly larger than the rms constant offset of 0.004 pixels expected from step-and-repeat errors [39].

Joffre and co-workers [14] noted that spectral interferograms or line spectra could be used to measure the MTF of a spectrometer-detector combination. Since we have measured both interferograms and the eLSF independently, we can test one against the other. Joffre and co-workers made their measurement in quasi-time, but we interpolate the eLSF (for a single wavelength) onto an evenly spaced frequency axis and Fourier transform to obtain the complex-valued fringe visibility ratio \hat{V}/V_{ideal} as a function of the time delay between pulses. The modulus $|\hat{V}/V_{\text{ideal}}|$ is compared with the recovered fringe amplitude (from the time domain fringe visibility, which is not equal to the quasi-time OTF) for that wavelength in interferograms at several time delays. Figure 5 compares these measurements at 764 nm and shows how the complex-valued fringe visibility adds delay dependent phase shifts exceeding 0.1 rad at 1 ps delay. Out to 3 ps delay, the

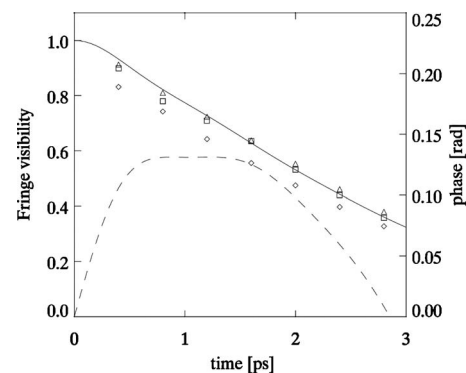


Fig. 5. Time domain fringe visibility ratio \hat{V}/V_{ideal} for the eLSF determined at 764 nm with the algorithm described in Subsection 3.B (solid line). The time domain fringe visibility ratio is calculated from the eLSF through a Jacobian transformation from wavelength to frequency followed by a Fourier transformation to the time domain. Since $V_{\text{ideal}} \approx 1$, the ratio is compared to experimental measurements of the fringe visibility for three sets of time delays (open squares, triangles, and diamonds). The temporal phase that results from placing the wavelength origin of the eLSF at its maximum is plotted as a dashed line.

agreement is 1.2% rms referenced to the maximum of the function. A systematic difference is seen in the slope of the two functions from 0.4 to 2.8 ps. This could be due to either nonlinearities in the CCD detector or the different smoothing characteristics of the quasi-time filtering versus the smoothing spline used to fit the eLSF in the wavelength domain. At larger time delays, the low amplitude structure in the fringe visibility is not well reproduced by the Fourier transform of the eLSF; similarly, the low amplitude wings of the eLSF will be more difficult to measure via the fringe visibility.

C. Spectrograph Calibration under Static Conditions

For the wavelength calibration of the spectrograph, the line spectra taken in conjunction with experimental data collection are fit to the nine final S_p shapes for the unblended argon lines. The line spectra were taken under the same conditions as those used to determine the eLSF and calibrated to the pixel axis with Eq. (7) [46]. On a time scale of hours, the calibration constants c_0 drift over a twentieth of a pixel, with a rms deviation (0.018 pixel) that is 2.5 times greater than their average standard error (0.0072 pixel) from single calibration fits. It is known that CCDs can move within their Dewar housings [29,49]. Comparisons of linear (c_1) and quadratic (c_2) calibration constants obtained over a time scale of hours do not reveal deviations greater than expected from their standard errors from single calibration fits [50]. We conclude that over the course of the experiment (~ 3 h) the position of the CCD array translates by one twentieth of a pixel. This motion is consistent with the thermal motion of the cooled CCD arrays detected previously [49]. The short term translation of the CCD array is not detectable through calibration spectra; the rms deviation of calibration constants for spectra taken within 5 min of one another is 0.0036 pixels. The translation of the CCD relative to the image can cause an apparent phase shift in a spectral interferogram by creating error in the calibration. We remove the slow translation of the CCD array by periodically recalibrating the spectrograph during data acquisition. The line spectra, recorded in groups of three and separated by 30 min, are recorded for both neon (Oriel model 6032) and argon lamps. The six argon spectra taken 30 min apart are used to calibrate the wavelength axis used for interferograms taken within the 30 min interval. The rms deviation of the argon spectra with these semi-local calibration axes is 0.010 pixels. The effect of residual drift and step-and-repeat errors of the wavelength axis from the semi-local axes can be estimated by using six unblended lines [51,52] in the neon spectra. The rms error of $\lambda_{\max} - \lambda_{\text{lit}}$ for the neon spectra on the semi-local axes is 0.003 nm (0.013 pixels).

D. Interferometer Construction and Stabilization

The pulses from a femtosecond Ti:sapphire laser with a ~ 40 nm wide spectrum were truncated to an ~ 0.5 mm diameter mode with an iris and then focused through a $200 \mu\text{m}$ pinhole by a 100 mm focal length plano-convex lens. The spatially filtered beam was collimated by a 200 mm focal length plano-convex lens over a distance of 2 m. After collimation, measured transmission through circular apertures could be fit to a Gaussian spatial intensity

profile of 1 mm 1/e diameter with a rms error of 1.5%. The Ti:sapphire polarization was rotated from horizontal to vertical with a zero-order half-wave plate so that broader bandwidth *s*-polarized beam splitters could be used in the interferometer. The spatially filtered pulses were sent into an actively stabilized Mach-Zehnder interferometer utilizing trihedral retroreflecting mirrors [35] for the movable mirrors in each arm (see Fig. 2). The interferometer was built on a $2' \times 2'$ internally damped breadboard, isolated from the floating optical table with rubber stoppers, and enclosed in a Plexiglas/lead-foam box to reduce air currents and acoustic noise. The area enclosed by the separated beams inside the interferometer was $\sim 20 \text{ cm}^2$.

The frequency and phase shift errors caused by the interferometer can be evaluated as follows. According to Eqs. 11–29 of [53] the solid angle of the source, as seen by the retroreflectors, is $1 \mu\text{rad}$. This yields an instrumental interferometer frequency error of $3 \times 10^{-7} \text{ rad/fs}$, which is less than 0.001 pixel. A beam displacement can be caused by the retroreflector moving at an angle to the beam as delay is changed. The alignment of the beam to the axis of the stage on which the retroreflector moves has an alignment error of less than 2° . This leads to a displacement of less than 0.03 mm for a 4 ps delay. Using a 0.03 mm displacement and the solid angle calculated from Eqs. 11–29 of [53] in Eq. 6.22 of [35] shows that the interferometer's phase shift must be less than $1 \mu\text{rad}$ over 2 ps of delay. Therefore, the effects of extended sources and beam displacements can be ignored.

The dielectric coated fused silica beam splitters (CVI, FABS-800-45S-PW-1025-UV) of the interferometer were chosen to be thick enough (6 mm) to fully separate multiple reflections at 45° from a 1 mm beam. This was necessary because the anti-reflection coatings of the beam splitters are not effective at the wavelengths of the CW lasers; multiple reflections of the red CW laser from thin beam splitters were found to make stabilization difficult. To minimize dispersion imbalance, the beam splitters were set parallel to within 0.2° by adjusting the angular deviation of reflections to within 5 mm over 150 cm. One arm of the interferometer had its length set with a computer controlled motorized translation stage (Newport MFN25PP, step size $\sim 0.1 \mu\text{m}$). The other arm was actively stabilized with a relatively stiff piezoelectric transducer (PZT) (Piezomechanik PST 150/10 \times 10/2, with a maximum displacement of $\sim 1 \mu\text{m}$ at $\sim 100 \text{ V}$) attached to a relatively light retroreflector (PLX OW-05-15, with a retroreflection accuracy of $5''$, trimmed to a mass of 3 g). The light retroreflector is needed to avoid mechanical resonances below 1 kHz, which could lie within the bandwidth of the servo system. For flat mirrors rather than retroreflectors mounted on PZTs, the expansion of the PZT was observed to change the beam angle. With fiber coupling, such a beam angle change in the interferometer introduces changes in the recorded spectrum of the pulse from that arm of the interferometer. In general, such an angular change can couple phase shifts and time delays, which cannot be distinguished with monochromatic light but can be distinguished by spectral interferometry [11,12].

Active stabilization was achieved through the generation of a feedback signal for the PZT. The feedback signal

was generated using a red CW laser (Melles–Griot 25-LHP-111-249, vacuum wavelength=632.9911±0.0007 nm) through the measurement of the intensity difference between the two interferometer outputs by focusing the output beams into a matched pair of photodiodes and analog signal subtraction. The intensity difference signal was conditioned by a loop filter (JILA electronics shop [54], operated in the −9 dB/CPU servo mode [55] with the −9 dB corner set at 10 Hz and the PI corner, where proportional gain turns into integral gain, set to 1 kHz) and a home built PZT driving amplifier before feedback to the PZT. The servo loop filter power was cycled with a rise/fall time of ∼1 s for changing the time delay in the interferometer with the translation stage. This servo system typically maintained a locked position for several hours if no change of delay was called for. In-loop measurements of the red intensity difference over several seconds suggest a stability of $\lambda/1000$, but servo-errors or the frequency drift of the red laser may cause the actual stability to be worse. The stabilization was measured out of loop with a yellow CW laser (Melles–Griot, 25-LYP-173-249, vacuum wavelength=594.6477±0.0006 nm). No attempt was made to stabilize the CW lasers in frequency or intensity. Relative shifts of the CW laser frequencies or loss of servo stabilization are evident as variations in the intensity difference between interferometer outputs for the 594.6 nm CW laser. The yellow intensity differences averaged on a 0.1 s time scale were monitored during the experiment; no interferograms in this data set had yellow intensity difference variations of greater than $\lambda/200$ at 594 nm. We record spectra of pulse pairs with known relative interferometer displacements of $j\lambda_{\text{cw}}/n_{\text{cw}}$, where j is an integer; λ_{cw} is the vacuum wavelength for the red CW laser used to lock the interferometer; and n_{cw} is the air index at λ_{cw} . The polarizer (Newport 11B00UP.25) on the Ti:sapphire output arm of the interferometer eliminates orthogonal polarization components that reduce the ideal fringe visibility in such a way that Eq. (1) would not apply. In this experiment, $V_{\text{ideal}} \approx 1$, so $\hat{V} \approx \hat{V}/V_{\text{ideal}}$. Before coupling the interferometer output into the single-mode fiber, one first surface reflection off a window (Fig. 2) is used in place of a mirror to reduce the CCD nonlinearity.

E. Data Processing

After background subtraction and flatfielding, pulse-pair spectra were subjected to a phase recovery algorithm as follows: (1) spectral restoration by pseudo-deconvolution with the eLSF; (2) subtraction of spectrally restored non-interfering spectra from each arm; (3) multiplication by the Jacobian [11,12] to transform from wavelength to frequency; (4) fast Fourier transformation to quasi-time; (5) isolation of the interference peak with the correct quasi-time delay using a filter; (6) inverse fast Fourier transformation back to pixel space; (7) calculation of the spectral phase difference, $\Delta\phi(\omega)$, from the complex-valued interferogram; (8) phase unwrapping; and (9) addition of integer multiples of 2π to give $-\pi < \Delta\phi(0) < \pi$. Note that the final frequency axis is unevenly spaced. If an evenly spaced frequency axis is required (for example, to reach the time domain), then the amplitude and phase are slowly varying and can be accurately interpolated as step 10 [11]. Note that the spectral restoration by pseudo-

deconvolution could be moved after step 4 to reduce computation, but this is not necessarily possible with other spectral restoration algorithms.

For this data set, the non-interfering pulse spectra for each arm subtracted in step 2 are scaled by $\pm 5\%$ to yield a zero-average result after the subtraction. Scaling factors may be due to the variation in shutter exposure time. The quasi-time filter in step 5 is a hyperbolic tangent,

$$f(\xi) = \{\tanh[(\xi - \xi_1)/5] - \tanh[(\xi - \xi_2)/5]\}/2, \quad (9)$$

where ξ_1 and ξ_2 were set 10 pixels wider than the points with 1% of the maximum amplitude on either side of the pixel with the maximum amplitude in quasi-time. The resulting interferogram is complex-valued, so that the phase modulation replaces the intensity modulation of the original interferogram. We recover the phase difference from the complex interferogram as $\Delta\phi(\omega) = \text{atan2}(\text{Re}[\hat{I}(\omega)], \text{Im}[\hat{I}(\omega)])$, where atan2 indicates the arctangent function with range $(-\pi, \pi]$ [56]. Unwrapping proceeds from the center of the spectrum and outward to the spectral wings to reduce random phase jumps where little intensity is present.

The recovered spectral phase differences $\Delta\phi(\omega)$ in Eq. (1) are affected by the differential dispersion of optical components in the interferometer and possibly other artifacts. $\Delta\phi$ can be precisely measured, but it is not accurately known in the experiments reported here. In contrast, the phase change between two phase differences,

$$\delta\Delta\phi(\omega) = \Delta\phi(\omega) - \Delta\phi_r(\omega), \quad (10)$$

is not affected by the differential dispersion if $\Delta\phi_r$ is a reference phase determined in the same interferometer. The actively stabilized interferometer with out-of-loop monitoring makes the spectral phase change accurately known:

$$\delta\Delta\phi(\omega) = \omega n(\omega) j \lambda_{\text{cw}} / (n_{\text{cw}} c) = \omega n(\omega) j T / n_{\text{cw}}, \quad (11)$$

where $n(\omega)$ is the refractive index of air [57]; λ_{cw} is the vacuum wavelength for the red CW laser used to lock the interferometer; n_{cw} is the refractive index of air at λ_{cw} ; c is the speed of light in vacuum; and j is the integer number of CW wavelengths (in air) by which the interferometer displacement is changed. The optical period of the locking laser is given by $T = \lambda_{\text{cw}}/c$. The reference phase is determined as the average difference phase for five interferograms at 545 fs delay. The phase delay,

$$\tau_\phi(\omega) = \delta\Delta\phi(\omega) n_{\text{cw}} / [\omega n(\omega)], \quad (12)$$

has often been used to measure the displacement with white light interferometry [7]. The accuracy of phase retrieval is evaluated here with the phase error,

$$e\phi(\omega) = \delta\Delta\phi(\omega) [n_{\text{cw}}/n(\omega)] - \omega j T, \quad (13)$$

and the phase delay error,

$$e\tau_\phi(\omega) = e\phi(\omega)/\omega. \quad (14)$$

The phase error and phase delay error are point by point measures of accuracy which directly reflect the accuracy of the phase retrieval for each pixel within the pulse spectrum. Small systematic errors in the phase or calibration can affect the measurements of parameters determined

from the phase such as the time delay, constant phase shift, or dispersion; the recovered phase changes were fit to polynomials to check for the influence of systematic errors. Following Albrecht *et al.* [11,12], the time delays and constant phase shifts were determined by a least-squares fit to lines:

$$\delta\Delta\phi(\omega)[n_{cw}/n(\omega)] = \omega\tau_s + \phi_0. \quad (15)$$

For positive frequencies, ϕ_0 is the negative of the time domain carrier-envelope phase shift [11]. The extrapolation to $\omega=0$ in fitting to an intercept phase shift, ϕ_0 , and slope delay, τ_s , is particularly sensitive to systematic errors in both the retrieved phase and the wavelength calibration. The slope delay error is

$$e\tau_s = \tau_s - jT. \quad (16)$$

Because no known source of constant phase change remained in the interferometer after switching to a piezo-mounted retroreflector, any deviation from the expected value of $\phi_0=0$ was taken as a constant phase error.

4. RESULTS AND DISCUSSION

A. Spectral Restoration

To assess the importance of spectral restoration to the algorithm, experimentally measured spectra were processed with and without spectral restoration. If the phase is extracted without spectral restoration, the average phase delay error over all time delays and all frequencies in the central 80 nm of the pulse spectrum is 0.8 as, with the worst case error of -33 as (at a single frequency in a single interferogram). The rms phase delay error across the entire data set is ± 10 as. Previous measurements of phase delay error by two-dimensional spectral shearing interferometry reported an accuracy of ± 35 as [58]. Figure 6 shows the phase delay error for two time delays; small systematic errors are evident.

The least computation-intensive spectral restoration is a deconvolution with the MTF, which requires a symmet-

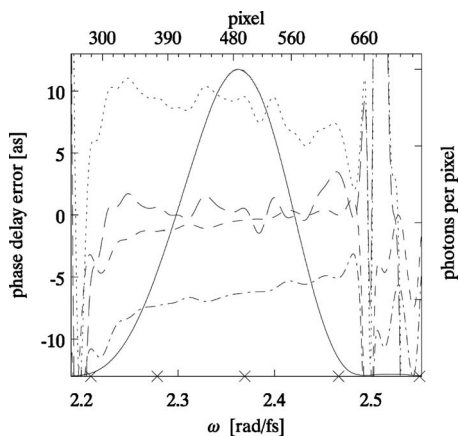


Fig. 6. Phase delay error in attoseconds for two different delays. Data are plotted both with and without spectral restoration with the eLSF. Delay time of 1915 fs: (dots) without spectral restoration and (long dashes) after spectral restoration. Delay time of 420 fs: without (dash-dot) and with (short dashes) spectral restoration. Intensity spectrum of Ti:sapphire pulse (solid line). The \times 's on the bottom horizontal axis indicate the frequencies of all unblended argon calibration lines in the range shown.

ric and pixel invariant eLSF. If the asymmetry and variation of the eLSF are ignored and spectral restoration proceeds by Fourier deconvolution with the MTF from the central eLSF, the phase delay error is changed from the no restoration case by less than 2 as. This means that even the 7% asymmetry and 12% width variation seen in the measured eLSF can bias the measurement of time delays less than 2 ps by 1 order of magnitude greater than the amount needed to recover accurate single-cycle pulse durations through spectral interferometry for direct electric-field reconstruction (SPIDER) [58].

Spectral restoration by pseudo-deconvolution with the eLSF shows several improvements over deconvolution with the MTF. Two measurements of the phase delay error are shown in Fig. 6 alongside the same phase delay errors determined without spectral restoration. The average phase delay error over all time delays is changed slightly to -0.8 as, with the worst case error showing a factor of 3 improvement to -10 as. The rms phase delay error for this data set is ± 2.5 as. This is very near to the $\lambda/1000$ (at 800 nm) stability expected from $\lambda/200$ stability criteria at 594.5 nm and the factor of 10 longer time for averaging the interferograms relative to the yellow laser measurements. Figure 7 shows an experimental interferogram without spectral restoration and one with spectral restoration. The restored interferogram displays improved fringe visibility and a shift in the phase. The shift in the phase arises from the asymmetry in the eLSF. The slight irregularities remaining in the restored fringe visibility are larger than expected from the shot noise and suggest additional instrumental imperfections (Subsections 4.B and 4.C).

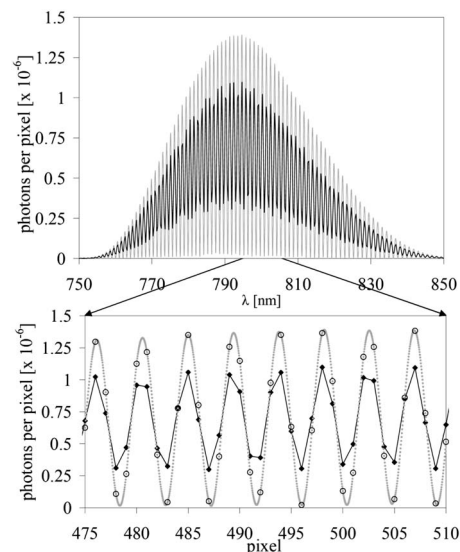


Fig. 7. The top panel compares the experimental interferogram I_p (black line) with the spectrally restored interferogram $I_0(\lambda_p)$ (gray line). Fourier pseudo-deconvolution with the complex valued OTF not only improves the fringe visibility, as seen in the top panel, but it shifts the phase of the interferogram as shown in the bottom panel. The bottom panel shows intensities from the raw interferogram (filled black diamonds) and the restored interferogram (open circles). The smooth curve (gray dots) for the restored interferogram was obtained by zero-padding in quasi-time. As a result of the asymmetric eLSF, the restored spectrum is shifted toward higher pixel numbers near several maxima and minima (for example, pixels 480 and 481; pixels 491 and 492; and pixels 502 and 503).

For comparison to prior work [14], the effect of spectral restoration algorithms on the precision of GDD measurements is given here. The GDD, ϕ'' , is measured as a quadratic fit to

$$\Delta\phi(\omega) = \phi_0 + \omega t + \phi'' \cdot (\omega - \bar{\omega})^2/2, \quad (17)$$

where $\bar{\omega} = 2.3530$ rad/fs. Without spectral restoration, the systematic phase delay errors in Fig. 6 result in a delay dependent GDD determination as seen by Dorrer *et al.* [14]. The GDD varies by up to 4 fs² depending on the time delay. Using deconvolution with the central MTF, the GDD shows the same variation with time delay as without spectral restoration. Using pseudo-deconvolution with the eLSF, no systematic trend is seen in the measurement of the GDD; the interferometer shows a GDD imbalance of -4.8 ± 0.2 fs². The precision is not improved over [10] for reasons discussed in Subsection 4.C.

B. Frequency Calibration Refinement

Examining the phase delay error, $e\tau_\phi(\omega)$, obtained by pseudo-deconvolution with the eLSF as a function of the time delay, a systematic growth in oscillatory features is apparent (see Fig. 8). This is not seen in simulations with a smooth calibration curve and the refractive index of air in the interferometer. *A priori*, this could arise from either a refractive index variation ($\Delta n \sim 10^{-6}$) with frequency in the interferometer or a calibration error variation ($\Delta\omega \sim 10^{-6}$ rad/fs) with frequency in the spectrograph. Assuming a refractive index variation, the Kramers–Kronig dispersion relations imply integrated atmospheric absorption strengths that are orders of magnitude too large [59,60], so the contribution from the refractive index variation must be negligible. This suggests that the accuracy could benefit from a refinement to the frequency axis that pushes the frequency accuracy beyond that achievable with a smooth calibration law based on a small set of spectral lines. The procedure presented here is inspired

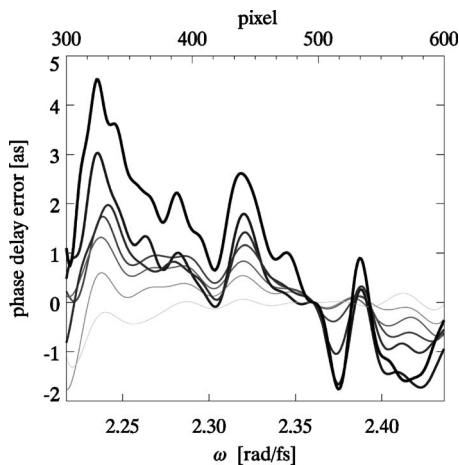


Fig. 8. Phase delay error in attoseconds for seven different delays after phase recovery algorithm on spectrally restored interferograms with the emission lamp frequency calibration described in Subsection 3.C. Lines grow in darkness and thickness with increasing delay: 270, 422, 545, 871, 1261, 1636, and 1959 fs. Each delay is normalized to reference pixel 496 and the oscillatory features are more pronounced as the delay increases. This translates to a calibration error, which requires the frequency calibration refinement algorithm described in Subsection 4.B.

by the frequency correction of Dorrer *et al.* [10,14], but differs in fitting linear dependence on the delay of the phase delay error for each pixel. The expected value of $\delta\Delta\phi(\omega)n_{\text{ew}}/n(\omega)$ is $\omega\tau_u$, where τ_u is the unknown true time delay, and ω is the unknown true frequency. The phase delay error then becomes

$$e\tau_\phi(\omega) = \omega\tau_u/[\omega - e\omega_p] - jT, \quad (18)$$

where $e\omega_p = (\omega - \omega_p)$ is the error in the frequency calibration for pixel p . Since the calibration is accurate to better than 0.02 pixels, we can make the approximation: $\omega/[\omega - e\omega_p] \approx 1 + e\omega_p/\omega$. Substituting this into the phase delay error gives $e\tau_\phi(\omega) = \tau_u - jT + \tau_u e\omega_p/\omega$. The difference between the actual and predicted time delay is removed by subtracting the phase delay error at a reference frequency ω_o , yielding the relative phase delay error,

$$e\tau_\phi(\omega_p) - e\tau_\phi(\omega_o) = \tau_u e\omega_p/\omega_p - \tau_u e\omega_o/\omega_o. \quad (19)$$

If a reference pixel (“o”) can be found where the frequency is known exactly [$e\omega_o = 0$] then $e\omega_p$ can be extracted from a fit of the phase delay error versus the slope delay τ_s ($\approx \tau_u$) for each pixel. In the limit of a known eLSF, the pixels with the best known frequencies have no time dependence for their relative phase delay error. The pixel that has the least correlation between the phase delay error and the time delay (pixel 496) is chosen as the reference pixel and its frequency error is assumed to be zero. The rms value of $e\omega_p$ determined in this way was 4×10^{-6} rad/fs or 0.005 pixels. This is consistent with the step-and-repeat errors expected from the fabrication of the CCD. The frequency refinement displays inflection points separated, on average, by 14 pixels, also suggesting step-and-repeat effects [39]. Unfortunately, due to the absence of Ne lines within the range of the frequency refinement [52], the Ne lines do not allow an independent experimental check on whether this procedure improves the calibration accuracy. When the above frequency calibration refinement is carried out on simulated spectral interferograms with Gaussian random step and repeat errors, the rms error of the wavelength calibration is reduced by a factor of 2; due to the filtered Fourier nature of the refinement, it has both overshoots and undershoots at the steps.

Because the extrapolation to find ϕ_0 is sensitive to systematic calibration errors, it provides a test of spectral restoration and of frequency refinement as a smoothed correction of discontinuous errors. Figure 9 shows the effect of spectral restoration and frequency calibration refinement on the constant (intercept) phase error. The least-squares fit to $\delta\Delta\phi(\omega) = \phi_0 + \omega\tau$ has been reported to display a systematic increase in the constant phase error of 1 rad for each picosecond of delay [11,12]. Without spectral restoration, the present results, shown in Fig. 9 (open diamonds), have a systematic phase error of 0.37 rad per ps. The factor of 3 improvement over [11,12] seen here is likely due to better frequency calibration. The maximum magnitude slope delay error is 227.4 as at 1959 fs delay. The slope delay error and constant phase shift error are strongly correlated; the constant phase shift error is systematically related to the slope delay error by $e\tau_s = -\phi_0/\omega_0$ with $\omega_0 = 2.356$ rad/fs (a frequency near the cen-

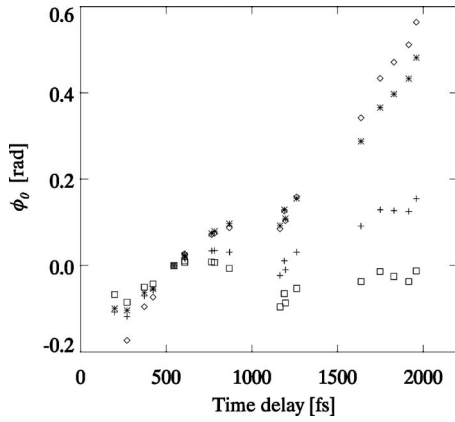


Fig. 9. Constant phase shift error versus absolute time delay. Open diamonds—raw data subjected to phase recovery algorithm; asterisks—phases recovered after Fourier deconvolution with the MTF from the central eLSF; crosses—data subjected to phase recovery algorithm after spectral restoration; open squares—phases recovered after spectral restoration and the frequency refinement algorithm described in Section 4.

ter of the pulse spectrum). The deconvolution with the MTF yields less than 20% improvement (Fig. 9, asterisks). The pseudo-deconvolution with the eLSF reduces the systematic trend in the constant phase errors by a factor of 3 to 0.12 rad per ps of delay; the slope delay error is correspondingly reduced by a factor of 3 to a maximum magnitude of 66.43 as at 1959 fs delay (Fig. 9, crosses). Refining the frequency axis with the above procedure before determining the constant spectral phase further decreases the systematic increase in constant phase error with increasing time delay (over 2 ps) to 0.006 ± 0.007 rad per ps of delay (Fig. 9, open squares). Over smaller delay ranges, a local variation of up to 0.08 rad over 800 fs still remains suggesting errors in the determination of the eLSF. This is a reduction in the systematic error by 2 orders of magnitude compared to [11,12]. The rms constant phase error is 0.05 rad. The slope delay error is reduced to an overall maximum magnitude of 40 as with a rms error of 19 as.

Fourier transform algorithms are not ideal for recovering step-and-repeat errors. Filtering in quasi-time inherently smoothes features in the wavelength domain, which is problematic for accurately recovering abrupt step-and-repeat errors. Without quasi-time filtering, a measurement of $e\omega_p$ is dominated by seemingly random noise. Sinusoidal patterns have been used previously to detect step-and-repeat errors in CCD arrays by nonlinear least-squares fitting [61]. The step-and-repeat error recovered by Fourier algorithms may be sufficient for treating data that have been recovered by the same algorithms, as they are both smoothed by the same quasi-time filtering operation (which varies with the time delay).

C. Interferometer Characterization

Except for brief comments about the GDD, the above results have focused on $\delta\Delta\phi(\omega)$, the spectral phase change, which is accurately known independently of the spectral interferograms. The discussion below focuses on the spectral phase difference $\Delta\phi(\omega)$, which contains information on the frequency dependent phase shift of the interferometer when the air paths in the two arms are equal. Be-

yond a dispersion imbalance expected from beam splitter thickness differences, the measured $\Delta\phi(\omega)$ contains expected contributions from the lock position of the stabilized interferometer [nominally $(j + \frac{1}{4})\lambda_{\text{CW}}$]. Therefore, $\Delta\phi(\omega)$ were fit to the sum of an air path difference and a beam splitter thickness difference,

$$\Delta\phi(\omega) - 2\pi m = \left(\frac{\omega n(\omega)}{c}\right)d + \left(\frac{\omega n_{\text{FS}}(\omega)}{c \cdot \cos[\theta_{\text{FS}}(\omega)]}\right)\delta t, \quad (20)$$

with a linear least-squares algorithm. In Eq. (20), $n(\omega)$ is the refractive index of air (calculated from the Sellmeier coefficients in [62] and the local atmospheric pressure ~ 0.816 atm); d is the interferometer path length difference in air between the two arms; c is the speed of light in vacuum; $n_{\text{FS}}(\omega)$ is the refractive index of fused silica (calculated from the Sellmeier coefficients in [63]); $\theta_{\text{FS}}(\omega)$ is the frequency dependent internal angle of the beam in the beam splitters calculated from Snell's law and $\theta_{\text{air}} = 45^\circ$; and δt is the fused silica beam splitter thickness difference between the two interferometer arms. Phase ambiguity modulo 2π in the experimental phase differences enables the subtraction of the nearest multiple m of 2π as determined from a preliminary least-squares fit with a constant term. From multiple interferograms, the average thickness difference δt_{avg} is $-167.3 \pm 0.5 \mu\text{m}$, which is within the manufacturer's thickness uncertainty of $250 \mu\text{m}$. This thickness difference is substantially different from that calculated with the ratio of the GDD over group velocity dispersion (GDD/GVD) ($\delta t = -116 \mu\text{m}$) because of the contribution from frequency dependent angles to the optical path length and temporal dispersion. The tenfold improved precision of this measurement relative to the thickness difference precision calculated for GDD precision/GVD [$(\pm 0.25 \text{ fs}^2 / (357 \text{ fs}^2/\text{cm})) \sim \pm 7 \mu\text{m}$] given in [10] derives from the exploitation of the constant phase shift information in this fit.

Using the average beam splitter thickness difference, δt_{avg} , tightens the error bars from individual phase difference fits for the air path difference, d , from ± 73.3 to ± 0.012 nm. These values of d were used to find the locking point of the interferometer. After substituting d , δt , and the red HeNe frequency into Eq. (20), the overall HeNe phase difference is divided by 2π to determine the difference in the number of HeNe waves between the interferometer arms at the locking point. The subtraction of the integer portion from each interferogram's number of HeNe waves yields 0.4071 ± 0.0012 waves, which is 0.1571 waves greater than the expected lock point of a quarter wave. This difference could be caused by imbalanced optical coatings in the interferometer (see below) or by electronic adjustments made to tighten the lock on the yellow HeNe. The lock precision of ± 0.0012 HeNe waves translates to an interferometer path length variation Δd of ± 0.76 nm. Between two interferograms, one would therefore expect $\delta\Delta d = \sqrt{2}\Delta d = 1.1 \text{ nm} = (0.0013)\lambda_{800 \text{ nm}}$; the $\delta\Delta d$ error of $(0.0009)\lambda_{800 \text{ nm}}$ from the spectrally restored data set (rms phase delay error of ± 2.5 as) is slightly smaller than expected based on fits to $\Delta\phi$ because the additional systematic spectral phase difference between arms in the interferometer is cancelled out when obtaining $\delta\Delta\phi$.

The phase residual $\Delta\phi_{\text{resid}}(\omega)$ is defined as the residual of the linear least-squares fit described by Eq. (20) and depends parametrically on the fit parameters δt , d , and m . The average and standard deviation of ten representative phase residuals are shown in Fig. 10. Since the expected standard deviation of the mean [64] phase residual is $\sqrt{10}$ smaller than the standard deviation of the phase residuals, Fig. 10 shows experimentally significant phase residuals (all less than ± 2 mrad) over most of the pulse spectrum. In Subsection 4.A, it was noted that the GDD precision had not improved over [10]; improvements in the GDD precision may be limited by these interferometer phase shifts with a more rapidly varying frequency dependence. Assuming the phase residuals represent interferometer phase differences, the derivative with respect to frequency of the phase residual gives the frequency dependent extra interferometer group delay. From $\Delta\phi_{\text{resid}}(\omega)$ in Fig. 10, the collection of representative interferograms has a group delay minimum of -0.7 fs and a maximum of 0.5 fs; thus, the data set's group delay falls within the range of ± 1.0 fs reported for a broader frequency range in a bare interferometer with dielectric beam splitters [65]. Differences between optical coatings on beam splitters may explain these group delay oscillations [66].

The standard deviation of the phase residual may approach the “standard quantum limit” (SQL) on interferometer phase measurements, $e\phi \geq 1/(2\sqrt{M})$, where M is the number of photons in the interferometer [67]. Figure 10 shows the frequency dependent SQL calculated by using the maximum number of detected photoelectrons at each pixel as M (in other words, M is proportional to the spectrum of the Ti:sapphire pulse in Fig. 6 with $\sim 1.4 \times 10^6$ photons at the peak of the spectrum). The read noise is insignificant compared to the shot noise over the frequency range shown in Fig. 10. The phase residual and SQL are quantitatively similar but differ in curvature. Processing of simulated spectral interferograms with small amplitude periodic interferometer phase shifts shows that some Fourier components of the interferometer phase shift can be strongly attenuated by the delay

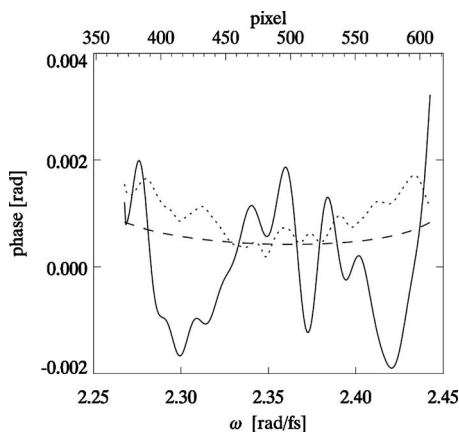


Fig. 10. The average phase residual (solid line) and standard deviation (dotted line) of ten interferograms ranging in delay from 199 to 1915 fs. The dashed line is the SQL for the phase uncertainty, $e\phi(\omega_p) = 1/[2\sqrt{M(\omega_p)}]$, where M is the mean number of photons in the interferometer detectable at pixel p .

dependent quasi-time filter in the FTSI algorithm, which might increase the phase residual. It is also not known whether the quantum limit for phase precision is reduced by the way the FTSI algorithm uses the whole spectrum and quasi-time filtering for phase retrieval. Figure 10 shows that the spectral phase difference $\Delta\phi$ from a single interferogram was retrieved with a rms precision of 1–2 mrad, so $\delta\Delta\phi$ should have a precision of 3 mrad, which exceeds the accuracy of interferometer stabilization (± 2.4 as, corresponding to 5 mrad).

5. CONCLUSION

The accuracy of spectral interferometry is dependent on knowledge of the calibration and effective linespread function of the pixelated wavelength resolving spectrograph and on knowledge of the phase shift of the bare interferometer. In grating spectrometers, the LSF is expected to be asymmetric and wavelength dependent due to coma and other aberrations. Here, a method used to measure the point-spread function for the Hubble Space Telescope was adapted to the measurement of the calibration and eLSF of a spectrograph with 0.013 pixel accuracy. Once measured, the eLSF can be used for spectral restoration of the interference spectrum before recovery of the unknown field by Fourier transform algorithms. The arbitrary choice of centering for an asymmetric eLSF has no effect on the restored spectrum so long as the same eLSF center is used for calibration and spectral restoration. When the wavelength dependence of the eLSF is slow, the pseudo-deconvolution algorithm can greatly increase the accuracy of Fourier transform spectral interferometry when both asymmetry and wavelength dependence of the eLSF are present. The accurately calibrated spectrograph provides information about frequency dependent interferometer phase shifts, including the constant term, which provides a more precise characterization of beam splitter thickness differences than the GDD alone. Using an actively stabilized interferometer with an external reference, it is demonstrated here that the displacement of an interferometer is measured to an accuracy of 0.72 nm over a range of 0.6 mm when the effective linespread function is accounted for in spectral interferometry. For time delays spanning 2 ps, the rms phase delay error is ± 2.5 as, limited by $\lambda/1000$ interferometer stability at 800 nm. The recovered phase changes have a precision of 2 mrad, with differences accurate to 7 mrad. This indicates the accuracy of the eLSF, calibration and spectral restoration, and FTSI measurements and algorithms. The present work experimentally demonstrates the stabilization and measurement of the phase delay to ± 2.4 as at around 1 ps delay (better than three parts in 10^6). Slope delays, however, show errors almost 1 order of magnitude larger. The constant (intercept) phase shift and slope delay are more sensitive to systematic errors in spectrograph calibration and interferometer alignment. Eliminating spurious phase shifts required an interferometer with retroreflectors in each arm, active stabilization using a retroreflector mounted on a piezoelectric transducer, and use of the interferometer to refine the spectrograph calibration between the atomic calibration lines. Combining all the above steps, for pulses with 43

nm FWHM bandwidth, the constant phase shift and slope delay are determined to accuracies of 0.05 rad and 19 as, respectively. Such accuracy in the constant phase shift will enable better characterization of optical components, improved pulse characterization via SPIDER [58,68,69], higher resolution surface profiling, and more accurate line shapes in 2D spectroscopy.

ACKNOWLEDGMENTS

We thank John L. Hall for his generous guidance in the construction of the stabilized interferometer and Veronica Vaida for helpful discussion of atmospheric absorption lengths and use of the high resolution Fourier transform spectrometer. Three of the authors (M. K. Yetzbacher, T. L. Courtney, and E. R. Smith) were partially supported by NSF-IGERT graduate traineeships through the Optical Science and Engineering Program at the University of Colorado. This work was funded by the Division of Chemical Sciences, Geosciences, and Biosciences, Office of Basic Energy Sciences of the U.S. Department of Energy (DOE) through grant DE-FG02-07ER15912.

REFERENCES AND NOTES

1. J. Walker, *The Analytical Theory of Light* (the Cambridge University Press, 1904).
2. L. M. Smith and C. C. Dobson, "Absolute displacement measurements using modulation of the spectrum of white light in a Michelson interferometer," *Appl. Opt.* **28**, 3339–3342 (1989).
3. J. Schwider and L. Zhou, "Dispersive interferometric profiler," *Opt. Lett.* **19**, 995–997 (1994).
4. J. Schwider and L. Zhou, "Dispersive interferometric profiler: erratum," *Opt. Lett.* **20**, 945 (1995).
5. L. Lepetit, G. Chériaux, and M. Joffre, "Linear techniques of phase measurement by femtosecond spectral interferometry for applications in spectroscopy," *J. Opt. Soc. Am. B* **12**, 2467–2474 (1995).
6. P. de Groot and L. Deck, "Surface profiling by analysis of white-light interferograms in the spatial frequency domain," *J. Mod. Opt.* **42**, 389–401 (1995).
7. P. Sandoz, G. Tribillon, and H. Perrin, "High-resolution profilometry by using phase calculation algorithms for spectroscopic analysis of white-light interferograms," *J. Mod. Opt.* **43**, 701–708 (1996).
8. D. N. Fittinghoff, J. L. Bowie, J. N. Sweetser, R. T. Jennings, M. A. Krumbügel, K. W. DeLong, R. Trebino, and I. A. Walmsley, "Measurement of the intensity and phase of ultraweak, ultrashort laser pulses," *Opt. Lett.* **21**, 884–886 (1996).
9. D. N. Fittinghoff, J. L. Bowie, J. N. Sweetser, R. T. Jennings, M. A. Krumbügel, K. W. DeLong, R. Trebino, and I. A. Walmsley, "Measurement of the intensity and phase of ultraweak, ultrashort laser pulses: erratum," *Opt. Lett.* **21**, 1313 (1996).
10. C. Dorrer, "Influence of the calibration of the detector on spectral interferometry," *J. Opt. Soc. Am. B* **16**, 1160–1168 (1999).
11. A. W. Albrecht, J. D. Hybl, S. M. Gallagher Faeder, and D. M. Jonas, "Experimental distinction between phase shifts and time delays: implications for femtosecond spectroscopy and coherent control of chemical reactions," *J. Chem. Phys.* **111**, 10934–10956 (1999).
12. A. W. Albrecht Ferro, J. D. Hybl, S. M. Gallagher Faeder, and D. M. Jonas, "Erratum: Experimental distinction between phase shifts and time delays: implications for femtosecond spectroscopy and coherent control of chemical reactions" [*J. Chem. Phys.* **111**, 10934 (1999)], *J. Chem. Phys.* **115**, 5691 (2001).
13. C. Dorrer, N. Belabas, J.-P. Likforman, and M. Joffre, "Spectral resolution and sampling issues in Fourier-transform spectral interferometry," *J. Opt. Soc. Am. B* **17**, 1795–1802 (2000).
14. C. Dorrer, N. Belabas, J. P. Likforman, and M. Joffre, "Experimental implementation of Fourier-transform spectral interferometry and its application to the study of spectrometers," *Appl. Phys. B* **70**, S99–S107 (2000).
15. S. K. Debnath, M. P. Kothiyal, and S.-W. Kim, "Evaluation of spectral phase in spectrally resolved white-light interferometry: comparative study of single frame techniques," *Opt. Lasers Eng.* **47**, 1125–1130 (2009).
16. A. A. Michelson and F. G. Pease, "Measurement of the diameter of an Orionis with the interferometer," *Astrophys. J.* **53**, 249–259 (1921).
17. M. Kakehata, H. Takada, Y. Kobayashi, K. Torizuka, Y. Fujihira, T. Homma, and H. Takahashi, "Single-shot measurement of carrier-envelope phase changes by spectral interferometry," *Opt. Lett.* **26**, 1436–1438 (2001).
18. E. Moon, C. Li, Z. Duan, J. Tackett, K. L. Corwin, B. R. Washburn, and Z. Chang, "Reduction of fast carrier-envelope phase jitter in femtosecond laser amplifiers," *Opt. Express* **14**, 9758–9763 (2006).
19. J. D. Hybl, A. Albrecht Ferro, and D. M. Jonas, "Two dimensional Fourier transform electronic spectroscopy," *J. Chem. Phys.* **115**, 6606–6622 (2001).
20. P. Baum, S. Lochbrunner, and E. Riedle, "Generation of tunable 7-fs ultraviolet pulses: achromatic phase matching and chirp management," *Appl. Phys. B* **79**, 1027–1032 (2004).
21. D. Meshulach, D. Yelin, and Y. Silberberg, "White light dispersion measurements by one- and two-dimensional spectral interference," *IEEE J. Quantum Electron.* **33**, 1969–1974 (1997).
22. M. A. Choma, M. V. Sarunic, C. H. Yang, and J. A. Izatt, "Sensitivity advantage of swept source and Fourier domain optical coherence tomography," *Opt. Express* **11**, 2183–2189 (2003).
23. From the standard deviation of the data in Fig. 6a of [10], the precision can be estimated as 0.25 fs².
24. J. Anderson and I. R. King, "Toward high-precision astrometry with WFPC2. I. Deriving an accurate point-spread function," *Publ. Astron. Soc. Pac.* **112**, 1360–1382 (2000).
25. T. P. Costello and W. B. Mikhael, "One-dimensional comparison of Wiener filtering and Richardson-Lucy methods for sectioned restoration of space-variant digital images," *IEEE Trans. Circuits Syst., I: Fundam. Theory Appl.* **49**, 518–522 (2002).
26. D. A. Fish, J. Grochmalicki, and E. R. Pike, "Scanning singular-value-decomposition method for restoration of images with space-variant blur," *J. Opt. Soc. Am. A* **13**, 464–469 (1996).
27. A. A. Sawchuk, "Space-variant image restoration by coordinate transformations," *J. Opt. Soc. Am.* **64**, 138–144 (1974).
28. W. H. Press, B. P. Flannery, S. A. Teukolsky, and W. T. Vetterling, *Numerical Recipes: The Art of Scientific Computing* (Cambridge U. Press, 1986).
29. S. B. Howell, *Handbook of CCD Astronomy*, 2nd ed., Cambridge Observing Handbooks for Research Astronomers (Cambridge U. Press, 2006).
30. The wavelength axis was given by $\lambda(p)=670\text{ nm}+(p-1)\cdot 0.5\text{ nm/pixel}$ for $p=1$ through $N=512$. The pulse spectrum was $|e(\lambda)|^2=(\lambda_0/\lambda)^2\exp[-(\lambda-\lambda_0)^2/2\sigma^2]$ with $\sigma^2=250\text{ nm}^2$ and $\lambda_0=800\text{ nm}$ (a FWHM of ~ 75 pixels on the 512 pixel array). The simulated eLSF for each pixel was a convolution of a pixel-centered Gaussian, $\exp[-(\mathcal{P}-p)^2/2\sigma^2]$, where $\sigma=0.53$ pixels is constant; a one-sided exponential decay, $\theta(p-\mathcal{P})\exp[-(p-\mathcal{P})/w_p]$; and a 1-pixel wide pixelation function. The final eLSF was repositioned with its maximum on the pixel center. The variation in the eLSF was created with the exponential width, $w_p=2-\tanh[(p-(N/2))/40]$, producing an eLSF FWHM ranging from 2 to 3.4 pixels.

31. The wavelength axis was given by $\lambda(p)=670 \text{ nm} + (p-1) \cdot 0.25 \text{ nm/pixel}$ for $p=1$ through $N=1024$. The eLSF was constructed in the same way described in note [30] except that $\sigma=0.21$ pixels and $w_p=0.675-(0.125)\tanh[(p-(N/2))/200]$, producing an eLSF FWHM ranging from 1.23 to 1.39 pixels, which was sufficiently undersampled on a grid of 1024 pixels.
32. J. Reader, "Optimizing Czerny-Turner spectrographs—a comparison between analytic theory and ray tracing," *J. Opt. Soc. Am.* **59**, 1189–1194 (1969).
33. E. Hecht, *Optics*, 2nd ed. (Addison-Wesley, 1990).
34. J. R. Janesick, *Scientific Charge-Coupled Devices* (SPIE, 2001).
35. W. H. Steel, *Interferometry, Cambridge Monographs on Physics* (Cambridge U. Press, 1967).
36. A. E. Siegman, *Lasers* (University Science Books, 1986).
37. F. A. Jenkins and H. E. White, *Fundamentals of Optics*, 4th ed. (McGraw-Hill, 1976).
38. R. D. Campbell and D. J. Thompson, in *Scientific Detectors for Astronomy 2005*, J. E. Beletic, J. W. Beletic, and P. Amico, eds. (Springer, 2005), pp. 507–514.
39. A. Reinheimer, e2v technologies, Tarrytown, NY (personal communication, March 11, 2008).
40. G. Steinmeyer, "Dispersion oscillations in ultrafast phase-correction devices," *IEEE J. Quantum Electron.* **39**, 1027–1034 (2003).
41. M. Downing, D. Baade, P. Sinclair, S. Deries, and F. Christen, *Proc. SPIE* **6276**, 627609 (2006).
42. A 0.05% sinusoidal ripple with a 14 pixel period is expected on the flatfield from this procedure. This is smaller than the shot noise on the interferograms. In principle, the expected ripple could be divided out of the flatfield, but simulated interferograms show that a 0.05% sinusoidal ripple in the flatfield causes less than 0.5 mrad phase ripple, so this was not done.
43. G. Norlen, "Wavelengths and energy-levels of Ar-I and Ar-II based on new interferometric measurements in region 3400–9800 Å," *Phys. Scr.* **8**, 249–268 (1973).
44. The argon lines used (from [43]) had the following vacuum wavelengths (in nanometers): 912.547 13, 867.032 50, 852.378 34, 826.679 43, 795.036 27, 763.720 78, 738.601 45, 727.494 00, and 696.735 19.
45. J. P. De Cuyper and H. Hensberge, "Wavelength calibration at moderately high resolution," *Astron. Astrophys. Suppl. Ser.* **128**, 409–416 (1998).
46. The polynomial was truncated at the quadratic term as the cubic term (predicted by the grating equation) was not well determined. Standard errors for the cubic coefficient, as estimated by least-squares fitting of single calibration spectra, were 30%–150% of its average value ($5 \times 10^{-11} \text{ nm/pixel}^3$). In contrast, the quadratic term was determined to within 1%–3% of its value ($4.8 \times 10^{-7} \text{ nm/pixel}^2$).
47. A. W. Fountain, T. J. Vickers, and C. K. Mann, "Factors that affect the accuracy of Raman shift measurements on multi-channel spectrometers," *Appl. Spectrosc.* **52**, 462–468 (1998).
48. V. Deckert and W. Kiefer, "Scanning multichannel technique for improved spectrochemical measurements with a CCD camera and its application to Raman-spectroscopy," *Appl. Spectrosc.* **46**, 322–328 (1992).
49. M. Gai, D. Carollo, M. Delbo, M. G. Lattanzi, G. Massone, F. Bertinotto, G. Mana, and S. Cesare, "Location accuracy limitations for CCD cameras," *Astron. Astrophys.* **367**, 362–370 (2001).
50. The standard deviation of the set of calibration constants c_1 is $2.0 \times 10^{-6} \text{ nm/pixel}$, smaller than the $4.4 \times 10^{-6} \text{ nm/pixel}$ average standard error estimated from the fits to individual spectra. The standard deviation of the set of calibration constants c_2 is $2.8 \times 10^{-9} \text{ nm/pixel}^2$, also smaller than the $1.8 \times 10^{-8} \text{ nm/pixel}^2$ average standard error of the fits to individual spectra. This means torsion or forward/backward motion of the CCD relative to the image plane is not detectable within the calibration precision and affects the calibration by less than the standard error of c_1 and c_2 .
51. K. Burns, K. B. Adams, and J. Longwell, "Interference measurements in the spectra of neon and natural mercury," *J. Opt. Soc. Am.* **40**, 339–344 (1950).
52. The neon lines in [51] are defined by vacuum wave numbers, which were inverted to wavelengths. The six lines used had the following vacuum wavelengths (in nanometers): 703.434 88, 717.591 20, 724.715 93, 744.094 35, 837.990 54, and 849.769 00.
53. R. J. Bell, *Introductory Fourier Transform Spectroscopy* (Academic, 1972).
54. The JILA loop filter was designed by J. L. Hall and T. Brown.
55. D. J. Jones, E. O. Potma, J. X. Cheng, B. Burfeindt, Y. Pang, J. Ye, and X. S. Xie, "Synchronization of two passively mode-locked, picosecond lasers within 20 fs for coherent anti-Stokes Raman scattering microscopy," *Rev. Sci. Instrum.* **73**, 2843–2848 (2002).
56. M. Metcalf and J. Reid, *Fortran 90/95 Explained* (Oxford U. Press, 1996).
57. G. Bönsch and E. Potulski, "Measurement of the refractive index of air and comparison with modified Edlen's formulae," *Metrologia* **35**, 133–139 (1998).
58. J. R. Birge, R. Ell, and F. X. Kartner, in *Ultrafast Phenomena XV*, P. Corkum, D. Jonas, R. J. D. Miller, and A. M. Weiner, eds. (Springer, 2006), pp. 160–162.
59. J. H. Seinfeld and S. N. Pandis, *Atmospheric Chemistry and Physics: From Air Pollution to Climate Change*, 2nd ed. (John Wiley & Sons, 2006).
60. The magnitude of the largest oscillation in the phase delay error (at $\sim 2.35 \text{ rad/fs}$ for 2 ps delay) gives a change in the real refractive index, Δn , on the order of 10^{-6} . From the Kramers–Kronig relationship, the change in the imaginary portion of the refractive index, $\Delta \kappa$, is approximately equal to Δn . By $\alpha=2\omega\kappa/c$, the absorption coefficient associated with the Δn from the $\Delta \phi$ can be found and inverted to an absorption length $l=1/\alpha=17 \text{ m}$, several orders of magnitude shorter than that of atmospheric O_2 or water vapor (see [59]).
61. S. Shaklan, M. C. Sharman, and S. H. Pravdo, "High-precision measurement of pixel positions in a charge-coupled-device," *Appl. Opt.* **34**, 6672–6681 (1995).
62. R. C. Weast and M. J. Astle, eds., *CRC Handbook of Chemistry and Physics*, 63rd ed. (CRC, 1982).
63. I. H. Malitson, "Interspecimen comparison of the refractive index of fused silica," *J. Opt. Soc. Am.* **55**, 1205–1209 (1965).
64. P. R. Bevington and D. K. Robinson, *Data Reduction and Error Analysis for the Physical Sciences*, 2nd ed. (McGraw-Hill, 1992).
65. M. Beck, I. A. Walmsley, and J. D. Kafka, "Group delay measurements of optical-components near 800 nm," *IEEE J. Quantum Electron.* **27**, 2074–2081 (1991).
66. J. Kim, J. R. Birge, V. Sharma, J. G. Fujimoto, F. X. Kartner, V. Scheuer, and G. Angelow, "Ultrabroadband beam splitter with matched group-delay dispersion," *Opt. Lett.* **30**, 1569–1571 (2005).
67. P. Hariharan and B. C. Sanders, in *Progress in Optics* (Elsevier Science, 1996), Vol. XXXVI, pp. 49–128.
68. C. Iaconis and I. A. Walmsley, "Self-referencing spectral interferometry for measuring ultrashort optical pulses," *IEEE J. Quantum Electron.* **35**, 501–509 (1999).
69. K. Yamane, Z. G. Zhang, K. Oka, R. Morita, M. Yamashita, and A. Suguro, "Optical pulse compression to 3.4 fs in the monocyte region by feedback phase compensation," *Opt. Lett.* **28**, 2258–2260 (2003).